Nanotechnology

PAPER

Geometric, electronic, and optical properties of MoS_2/WSSe van der Waals heterojunctions: a first-principles study

To cite this article: Yan-Fang Zhang *et al* 2021 *Nanotechnology* **32** 355705

IOP Publishing Nanotechnology
Nanotechnology 32 (2021) 355705 (9pp) https://doi.org/10.1088/1361-6528/ac0569

Geometric, electronic, and optical properties of MoS_2/WSSe van der Waals heterojunctions: a first-principles study

Yan-Fang Zhang[1], **Jinbo Pan**[1] and **Shixuan Du**[1,2,3,*]

[1] Institute of Physics and University of Chinese Academy of Sciences, Chinese Academy of Sciences, Beijing 100190, People's Republic of China
[2] CAS Center for Excellence in Topological Quantum Computation, University of Chinese Academy of Sciences, Beijing 100190, People's Republic of China
[3] Songshan Lake Materials Laboratory, Dongguan, Guangdong 523808, People's Republic of China

E-mail: sxdu@iphy.ac.cn

Received 2 February 2021, revised 6 May 2021
Accepted for publication 26 May 2021
Published 11 June 2021

Abstract

Van der Waals (vdW) heterojunctions constructed by vertical stacking two-dimensional transition metal dichalcogenides hold exciting promise in realizing future atomically thin electronic and optoelectronic devices. Recently, a Janus WSSe structure has been successfully synthesized by using chemical vapor deposition, selective epitaxy atomic replacement, and pulsed laser deposition methods. Herein, based on first-principles calculations, we introduce the structures and performances of MoS_2/WSSe vdW heterojunctions with different interfaces and stacking modes. The vdW heterojunctions possess indirect band gaps for S–S interfaces, while direct band gaps for Se–S interfaces. Besides, the potential drop indicates an efficient separation of photogenerated charges. Interestingly, the opposite built-in electric fields formed in the vdW heterojunctions with a S–S interface and a Se–S interface suggest different charge transfer paths, which would motivate further theoretical and experimental investigations on charge transfer dynamics. Moreover, the electronic property is adjustable by applying external in-plane strains, accomplishing with indirect to direct bandgap transition and semiconductor to metal transition. The findings are helpful for the design of multi-functional high-performance electronic and optoelectronic devices based on the MoS_2/WSSe vdW heterojunctions.

Keywords: MoS_2/WSSe vdW heterojunctions, first-principles calculations, band engineering, nano-electronics and opto-electronics

(Some figures may appear in colour only in the online journal)

1. Introduction

Quantum confinement and surface effect endow two-dimensional materials exhibiting unique electronic and optical properties [1–5]. Two-dimensional transition metal dichalcogenides (TMDs), MoS_2, and some of its Janus structures, almost as thin, transparent, and flexible as graphene [6–8], have opened the realm of ultrathin and flexible electronic and photonic applications due to their intrinsic semiconductive property, including but not limited to direct bandgap [9], high carrier mobility [10], and strong light-matter interactions [11]. The above-mentioned electronic and optical properties can be tuned by layer thickness, external electric/magnetic field, and strains [12–15]. Furthermore, vertical stacked van der Waals (vdW) heterojunctions, which inherit the intrinsic properties of the building blocks and create particular applications at the same time, have been envisioned to play a key role in the area of optoelectronic functions including photodetection, photovoltaics (PV), light-emitting diodes, water-splitting photocatalysts [2, 16–26], and so on.

Researches on TMDs vdW heterojunctions are mainly focused on MX_2/MX_2 and MX_2/MXX' forms (M = Mo,

* Author to whom any correspondence should be addressed.

W, X, X′ = S. Se. Te, X′≠X) [19, 27–31]. These vdW heterojunctions present attractive properties, ultrafast charge separation in $MoS_2/MoSe_2$ [29], long-lived interlayer excitons in $MoSe_2/WSe_2$ [28], and negative differential transconductance in MoS_2/WSe_2 [27], to name a few. Inspired by the recent fabrication of WSSe monolayer [32, 33], possible applications of the MoSSe/WSSe vdW heterojunctions in valleytronics and optoelectronics [34–37] have been reported.

In this work, using density functional theory based first-principles calculation, we systematically investigated the MoS_2/WSSe vdW heterojunctions with S–S interfaces and Se–S interfaces in AA and AB stacking modes. Though there are negligible differences in optimized lattice constants and total energies for all the four vdW heterojunctions, the electronic properties are varied. The vdW heterojunctions with S–S interfaces are indirect bandgap semiconductors, while those with Se–S interfaces are direct bandgap semiconductors. The potential drop between the two layers in the vdW heterojunction induces a built-in electric field across the interface, promoting the separation of the photogenerated electron-hole pairs. The vdW heterojunctions with S–S interface and Se–S interface both exhibit appealing optical absorbance properties in the visible light region with different electron transfer mechanisms. The electronic properties are notably tuned by strains, realizing semiconductor-metal transitions.

2. Methods

All the calculations were performed by using first-principles calculations based on density functional theory as implemented in the Vienna *Ab initio* Simulation Package (VASP) with the projector-augmented wave method [38, 39]. A plane-wave basis with a cutoff energy of 500 eV was used [40]. The structures were fully relaxed with an energy convergence threshold of 10^{-6} eV and residual forces of less than 10^{-2} eV Å^{-1}. The gamma-centered k point sampling of $15 \times 15 \times 1$ was adopted. The heterojunctions are combined with 1×1 MoS_2 stacking on 1×1 WSSe. All the configurations are fully relaxed with the Perdew–Burke–Enzerhof exchange-correlation functional. The strains considered in this work are all in-plain biaxial strains. Heyd–Scuseria–Ernzerhof (HSE06) hybrid functional was adopted to get more accurate band structure and optical absorbance [41]. The optb88 corrections were used to consider the vdW interactions between the two layers in the systems [42]. The dipole corrections perpendicular to the interfaces of the vdW heterojunctions were considered [43]. The electronic potential was obtained by averaging the potential values by the number of grid points perpendicular to the z direction.

The binding energy is used to estimate the stability of the vdW heterojunctions, with the following definition:

$$E_b = E_{MoS_2} + E_{WSSe} - E_{MoS_2/WSSe}$$

in which the E_{MoS_2}, E_{WSSe}, and E_{MoS_2}/WSSe are the total energies of monolayer MoS_2, WSSe, and the MoS_2/WSSe vdW heterojunction, respectively.

The optical absorption spectrum was derived by determining the frequency-dependent dielectric tensor matrix using density functional perturbation theory [44, 45]. The following equation has been used to get the optical absorption spectrum:

$$A(\omega) = 1 - e^{-\alpha(\omega)\cdot\Delta z}$$

in which

$$\alpha(\omega) = \frac{\sqrt{2}\,\omega}{c}\left[\sqrt{\varepsilon_1^2 + \varepsilon_2^2} - \varepsilon_1\right]^{\frac{1}{2}}$$

describes the absorption coefficient. The ε_1 and ε_2 are the real and imaginary parts of the dielectric function, respectively. ω is the light frequency. c is the speed of light in vacuum. Δz is the unit-cell size in the z direction.

3. Results and discussions

Considering that the bulk MoS_2 in a 2H phase is the most common form in nature and the monolayer MoS_2 in 1H phase is a semiconductor with a direct bandgap character, the monolayer MoS_2 and WSSe in the following discussion are both in 1H phase. As shown in figure 1, there are two different interfaces for MoS_2/WSSe vdW heterojunction, S–S interface, and Se–S interface, respectively. Four configurations with different interfaces and stacking modes were investigated, named as S–S-AA, S–S-AB, Se–S-AA, and Se–S-AB. For the AA stacking structure, the anions in the top monolayer material are right over the anions in the bottom monolayer material, resulting in a honeycomb structure. It is different for the AB stacking structure with the anions in the top monolayer material pointing to the cations in the bottom monolayer material. Since the monolayer MoS_2 and WSSe have been successfully fabricated in experiment [9, 32, 33], the structure stability is not discussed here. The lattice constants show negligible differences for all the four vdW heterojunctions. The interlayer distances vary from 3.05 Å (S–S-AB) to 3.71 Å (Se–S-AA), indicating weak vdW interactions at the interface. AA stackings have larger interlayer distances (3.64 Å for S–S interface and 3.71 Å for the Se–S interface), mainly due to the repulsive electrostatic interaction between the anions at the interface. The positive binding energies presented in table 1 indicate that the four MoS_2/WSSe vdW heterojunctions are all stable.

The electronic structures of the four vdW heterojunctions are presented in figure 2. The four vdW heterojunctions are all type-II heterojunctions. It is interesting to note that the vdW heterojunctions with S–S interfaces are indirect bandgap semiconductors (figures 2(a) and (b)) with the valence band maximum (VBM) locating at the Γ point and the conduction band minimum locating at the K point. However, the vdW heterojunctions with Se–S interfaces are direct bandgap semiconductors (figures 2(c) and (d)) and their CBMs and VBMs reside at the K point. The calculated band gaps are summarized in table 1. The VBM positions of the S–S-AA, S–S-AB, Se–S-AA, Se–S-AB heterojunctions relative to the vacuum level of the WSSe layer are −5.62 eV, −5.40 eV, −6.47 eV, and −6.48 eV, respectively. The band gaps are all

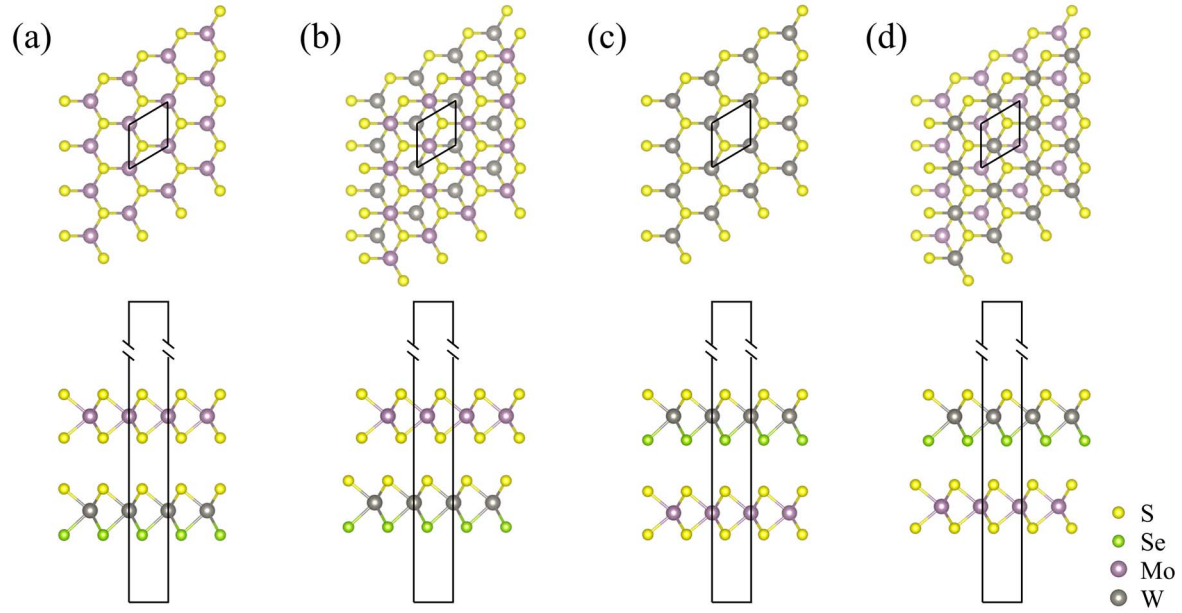

Figure 1. Top and side views of the geometric structures for MoS_2/WSSe vdW heterojunctions with S–S interfaces, Se–S interfaces, and AA, AB stackings (from left to right).

Table 1. Lattice parameters, binding energies, band gaps, and electron transfers for the four MoS_2/WSSe vdW heterojunctions.

	S–S-AA	S–S-AB	Se–S-AA	Se–S-AB
Lattice constant (Å)	3.22	3.23	3.22	3.23
Interlayer distance (Å)	3.64	3.05	3.71	3.15
S/Se–S distance (Å)	3.64	3.56	3.71	3.66
Binding energy (meV)	171	228	172	225
E_{g_dir} (eV)	1.71	1.66	1.00	1.09
E_{g_indir} (eV)	1.59	1.33	—	—
Electron transfer ($\|e\|$)	−0.002	0.0002	0.004	0.009

relatively smaller than those of pristine monolayer MoS_2 (∼2 eV [46, 47]) and WSSe (∼2.13 eV [48]). The CB and VB mainly contributed by orbitals from different layers further confirm the weak vdW interaction between the two monolayers.

Due to the different electronegativity of S and Se atoms, there is electron transfer between the two layers even though the interlayer interaction is weak. The Bader charge analysis reveals that the electron losses of the monolayer WSSe are −0.002, 0.0002, 0.004, and 0.009 *e* for S–S-AA, S–S-AB, Se–S-AA, and Se–S-AB heterojunctions, respectively. The electron loss can be used to explain the reason for the smaller bandgap in the vdW heterojunction with Se–S interface than that with S–S interface. For the vdW heterojunction with Se–S interface, the electron loss from the WSSe layer to the MoS_2 layer results in the upward shifts of the valence band and the downward shifts of the conduction band, thus a smaller bandgap. On the contrary, the heterojunctions with the S–S interface have larger band gaps.

In the S–S-AA vdW heterojunction, an electrostatic potential drop $\Delta\Phi$ around 0.75 eV is observed from the MoS_2 monolayer to the WSSe monolayer. The electrostatic potential drop direction indicates that electron transfer from MoS_2 to WSSe occurs, matching well with the Bader charge analysis. The potential drop between the two layers induces a large built-in electric field across the interface, pointing from MoS_2 to WSSe. However, there is a built-in electric field pointing from the WSSe layer to the MoS_2 layer due to an opposite potential drop direction (figure 3(b)) for the Se-S-AA vdW heterojunction.

The built-in electric field plays a crucial role in separating the photogenerated electron-hole pairs, which is beneficial for photocatalytic applications. Figures 3(c) and (d) illustrate the electron transfer mechanism for the S–S-AA vdW heterojunction and the Se–S-AA vdW heterojunctions respectively. In the two vdW heterojunctions, due to the intralayer absorption, the electrons from the valence band of MoS_2 (WSSe) would excited to the conduction band of MoS_2 (WSSe), leaving holes at the valence band and electrons at the conduction band of MoS_2 (WSSe). Next, for the S–S-AA vdW heterojunction, the built-in electric field promotes the photogenerated electrons (holes) to migrate to the MoS_2 (WSSe) layer. However, the built-in electric field in the Se–S-AA vdW heterojunction facilitates the electrons transition from the conduction band in the MoS_2 layer to the valence band in the WSSe layer, probably resulting in a direct

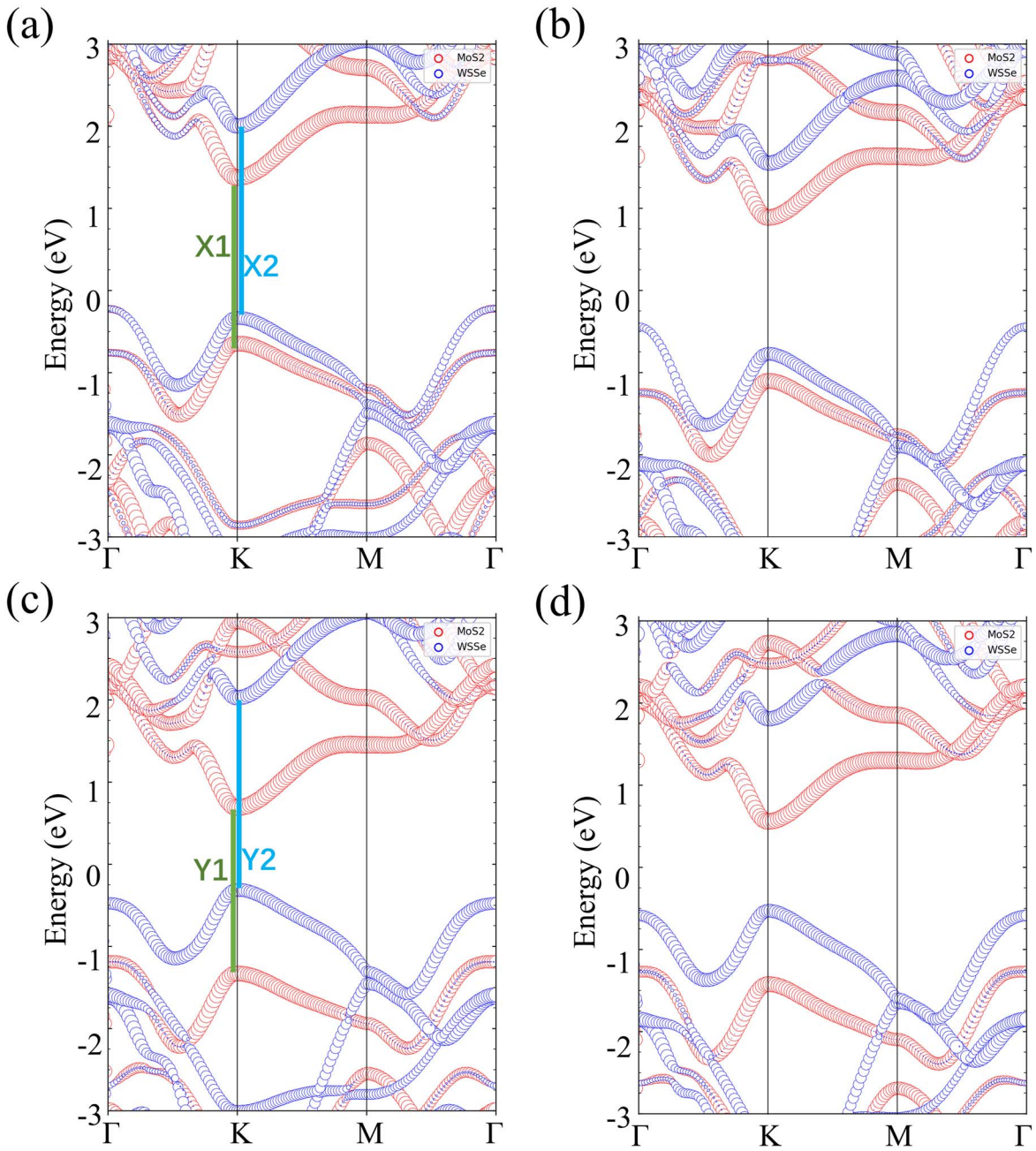

Figure 2. Projected band structures of the four MoS_2/WSSe vdW heterojunctions (a) S–S-AA vdW heterojunction, (b) S–S-AB vdW heterojunction, (c) Se–S-AA vdW heterojunction, (b) Se–S-AB vdW heterojunction. The red and blue circles present the contributions from the MoS_2 layer and the WSSe layer, respectively. X1, X2, Y1, and Y2 are the intralayer transition paths related to the first two optical absorption peaks.

Z-scheme photocatalyst. Considering that the photocatalytic mechanism is a balance of the built-in electric field, Coulomb repulsion, and potential difference at the interface [49], further theoretical and experimental investigations are required to determine the exact photocatalytic mechanism in the MoS_2/WSSe heterojunction with different interfaces, such as the competition between the photogenerated carrier relaxation and recombination, and *ex* and *in situ* irradiated x-ray photoelectron spectroscopy characterization of the charge carrier migration.

The ability to harvest solar light, especially the visible and near-infrared regions, is required to produce high-efficiency photovoltaic and photocatalytic devices. Therefore, we investigated the optical-absorption performance of the vdW heterojunctions with the two interfaces in an AA stacking mode. As displayed in figures 3(e) and (f), both of the two vdW heterojunctions exhibit excellent light absorption performance in the visible region and the near-ultraviolet region. Two high peaks around 2.35 and 2.72 eV indicate a great potential to be used in photovoltaic and photocatalytic devices.

The optical properties of the heterojunctions are due to the response of the system to a time-dependent electromagnetic perturbation. The optical complex dielectric

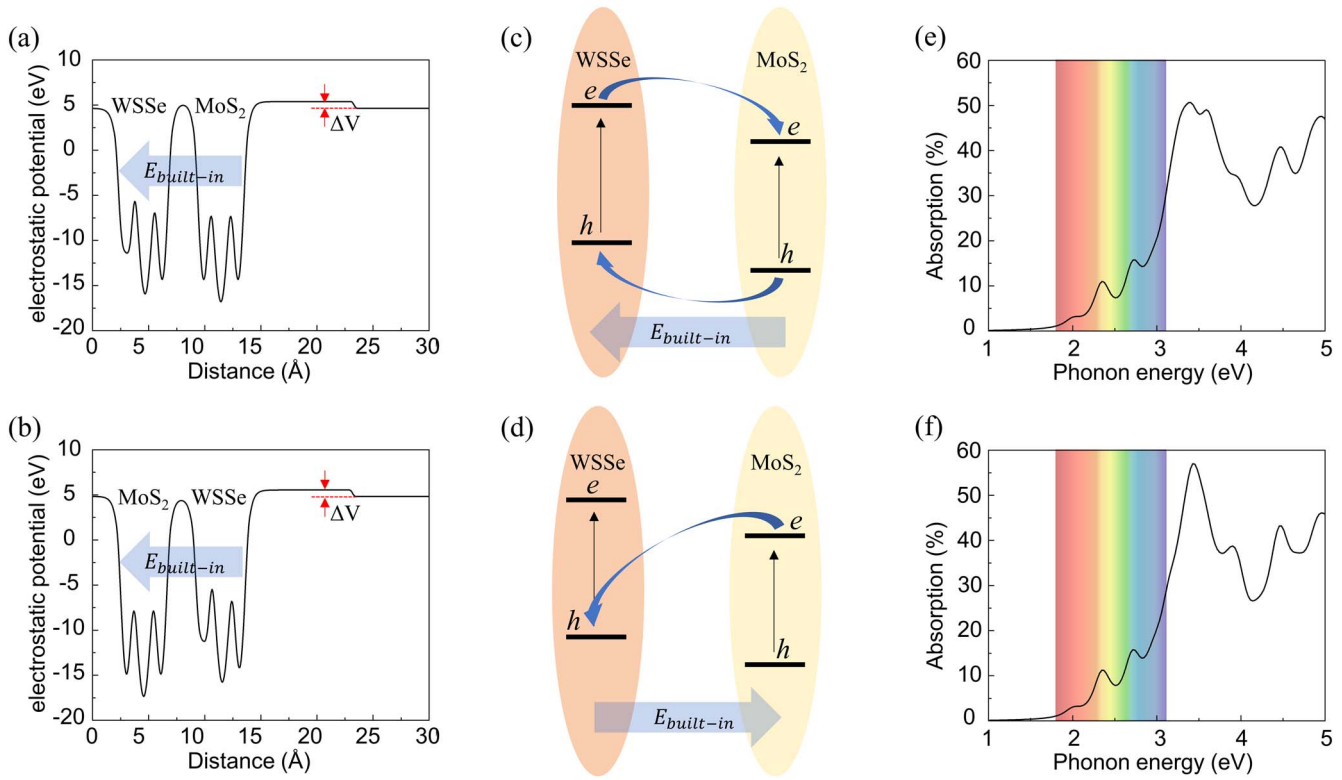

Figure 3. (a) and (b) Electrostatic potentials of the S–S-AA and Se–S-AA vdW heterojunctions along the z direction. (b) and (d) Possible schematic diagrams of the S–S-AA and Se–S-AA vdW heterojunctions. (e) and (f) Optical absorption spectrum of the S–S-AA and Se–S-AA vdW heterojunctions.

function consists of 'interband' and 'intraband' contributions. Due to the depolarization effects [50], the 'interband' absorption gives a negligible contribution, and the optical absorption as shown in figures 3(e), (f) thus mainly contributed by the intraplane transition of MoS_2 and WSSe. Even though the two MoS_2/WSSe heterojunctions with different interfaces have different band structures around Fermi energy, their optical absorptions are almost the same in the visible light region. There are three peaks in the optical absorption spectra in the visible light range for both heterojunctions. The first two peaks are contributed by the intralayer transition X1 and X2 (or Y1 and Y2, shown in figures 2(a), (c)), while the third one is resulted from a superposition of multiple transition paths at different k points.

Interestingly, the potential drop can effectively be tuned by external strains, as depicted in figure 4. For all the four studied systems, a linear decreasing of the potential drop with strain is observed. This phenomenon suggests that external compressive strains enhance the built-in electric field, and thus improve the electron-hole separation performance.

External strains on two-dimensional semiconductors influence not only the electrostatic potential drop but also other electronic properties and thereby optical properties. Next, we investigated other electronic properties responses to biaxial strains ranging from −8% to 8%. The negative values mean compressive strains, while the positive ones mean tensile strains. Figure 5 gives the bandgap variation under different strains. The bandgap variation for all the four vdW heterojunctions shows the same trend from compressive

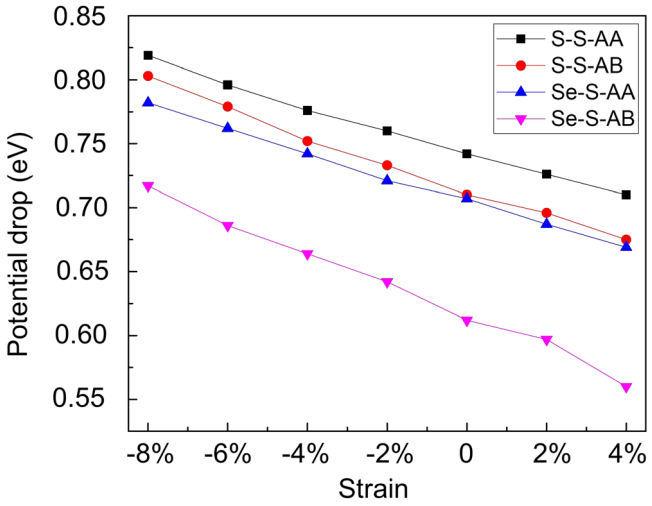

Figure 4. Potential drop for the four vdW heterojunctions under biaxial compressive and tensile strains.

strains to tensile strains. With the decreasing of compressive strains, the value of the bandgap increases. The bandgap reaches its maximum at ∼4% compressive strain, and then it decreases gradually. The heterojunctions tend to have a direct bandgap at −2% strain. Although the vdW heterojunction with the S–S interface and AB stacking is still a semiconductor, the direct and indirect bandgap difference is only 91 meV. Thus, a direct bandgap can be expected at around the −2% compressive strain. At large tensile strains, the heterojunctions change from semiconductors to metals. For

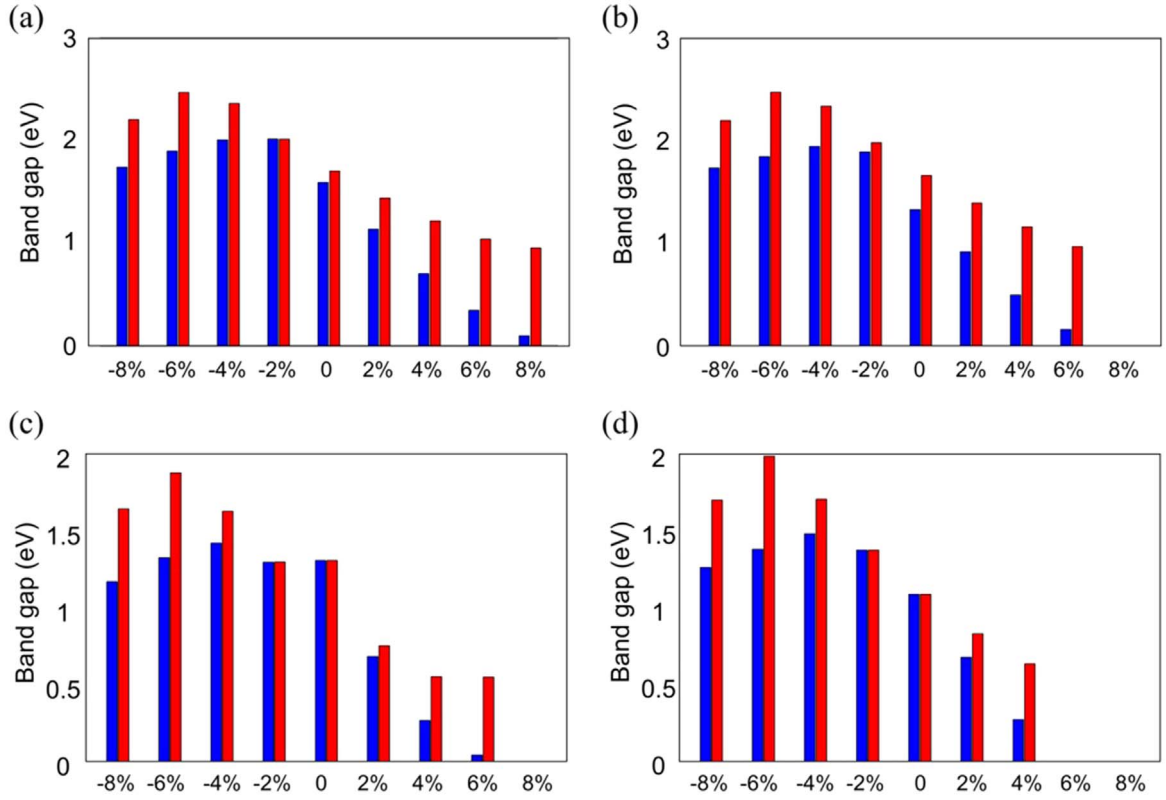

Figure 5. Indirect (blue) and direct (red) band gaps for the four vdW heterojunctions under biaxial compressive and tensile strains (a) S–S-AA vdW heterojunction, (b) S–S-AB vdW heterojunction, (c) Se–S-AA vdW heterojunction, (b) Se–S-AB vdW heterojunction.

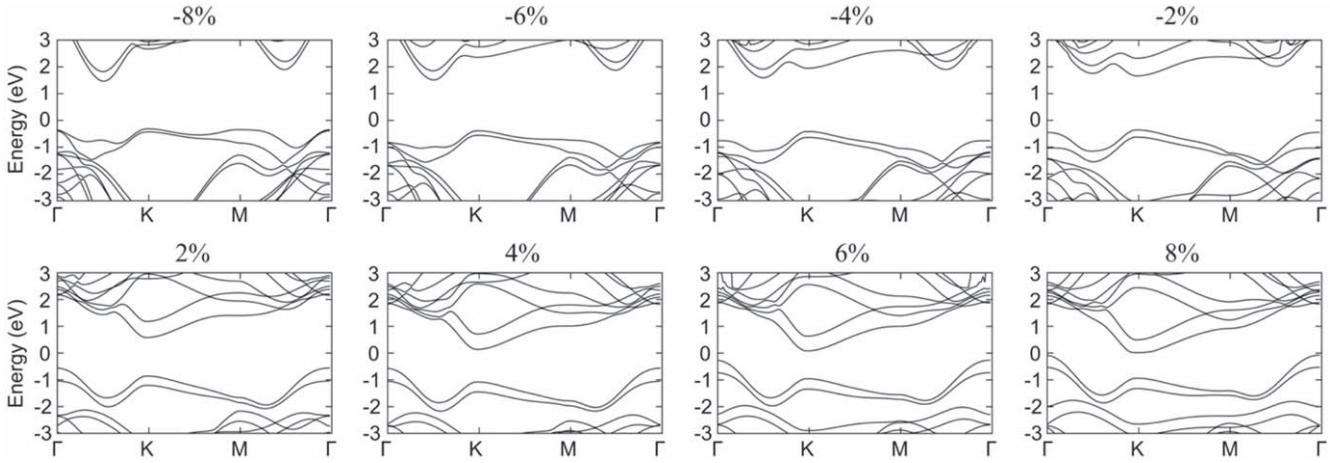

Figure 6. Band structure variations of the S–S-AA vdW heterojunction under biaxial compressive and tensile strains.

example. The vdW heterojunction with the Se–S interface and AB stacking is metal under 6% strain.

Taking the vdW heterojunction with S–S interface and AA stacking as an example, figure 6 presents more clearly about the band structure variation under biaxial tensile and compressive strains. From compressive strains to tensile strains, the CBM moves down to get close to the Fermi level, resulting in a smaller and smaller bandgap. During this variation process, the CBM changes from a point between Γ and K to K point. In addition, the VBM moves from the K point to the Γ point. The change of the CBM and VBM positions leads to an indirect-direct-indirect band gap transition under strains, demonstrating that applying external strains can effectively modulate the band structures of the MoS_2/WSSe vdW heterojunctions. The external strain effect can be achieved in an experiment by applying external load or stress on the heterojunction, bending, or the lattice mismatch between the heterojunction and the substrate [51–54].

To elucidate the band structure evolution of MoS_2/WSSe heterojunction with S–S–AA interface under various strains, we calculated the charge density distributions of the heterojunction on four key sites (figure 7), CB (Γ–K), CB (K), VB (Γ), and VB (K). Therein, CB (Γ–K), CB (K), VB (Γ), and VB (K) are the conduction band between high symmetry

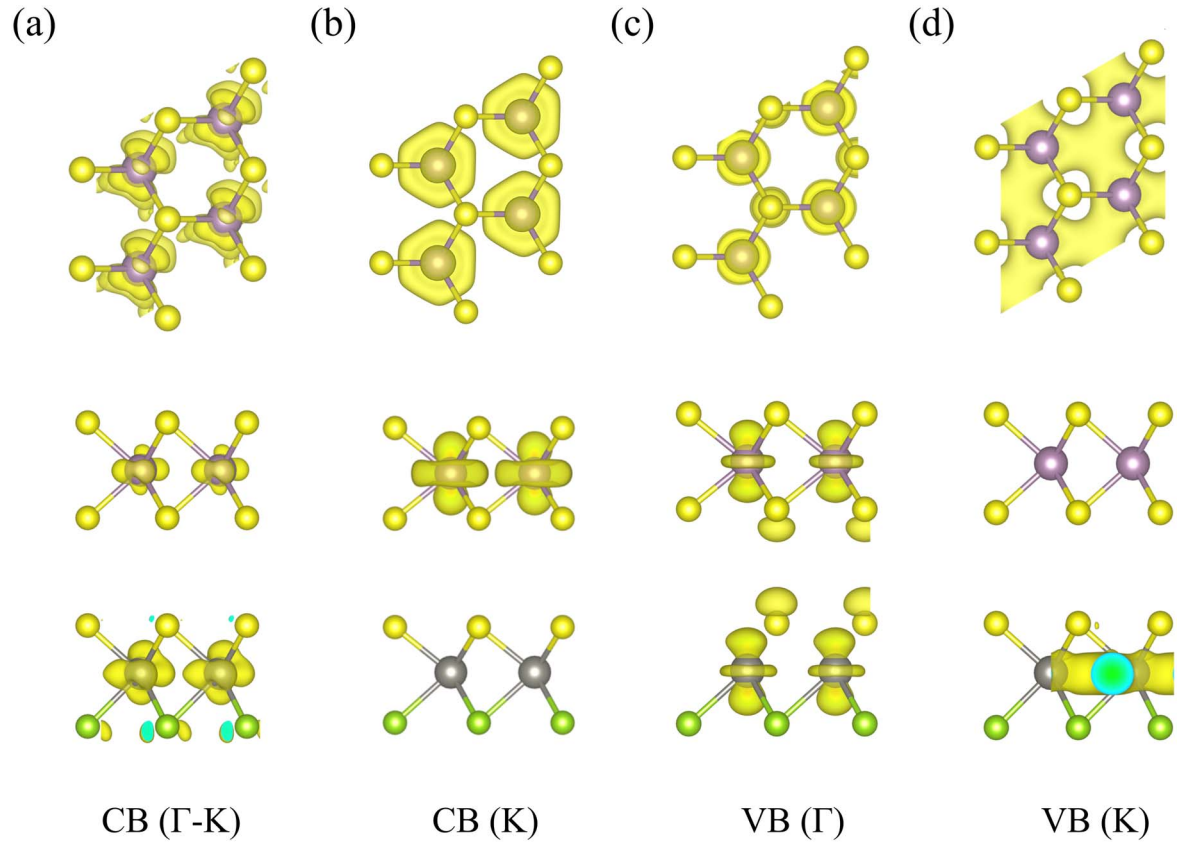

Figure 7. Top and side views of the charge density distributions of the S–S-AA vdW heterojunction on CB (Γ–K), CB (K), VB (Γ), and VB (K).

point Γ and K, conduction band at K point, valence bands at Γ and K points, respectively. As can be seen, the charge density distributions at CB (Γ–K) mainly contributed by in-plane 3*d*-orbitals of W atoms, and that at CB (K) contributed by both in-plane and out-plane orbitals. While the charge density distributions at VB (Γ) mainly contributed by the out-plane d_z^2 orbital of W atoms, and that at CB (K) mainly contributed by the in-plane 3*d*-orbitals of W atoms. According to previous literature, different orbitals have different responses to strain, and the band evolution under strain results from the competition between the electron-ion interaction and the electron-electron interaction [55]. Qualitatively, the orbitals interaction at CB (Γ–K) is larger than that at CB (K), resulting in a larger response of the band at CB (Γ–K) to the strain, and the band goes up as strain increases. Similarly, a larger orbital interaction occurs at VB (K) than that at VB (Γ), and the band goes down asstrain increases.

4. Conclusion

Using first-principles calculations, we demonstrate that despite the very close lattice constants and system energies, the MoS_2/WSSe vdW heterojunctions with S–S interfaces and Se–S interfaces possess indirect band gaps and direct band gaps, respectively. The vdW heterojunctions effectively promote the separation of the photogenerated electron-hole pairs due to the large built-in electric field across the interface. Different photocatalyst mechanisms may exist in the MoS_2/WSSe heterojunctions with different interfaces, which need further theoretical and experimental validations. The heterojunctions show excellent ability to absorb solar energy in the visible region, indicating good optical absorption performance. All the MoS_2/WSSe vdW heterojunctions experience indirect-direct-indirect transitions from compressive strains to tensile strains, and transit to metals under large tensile strains. The as-demonstrated MoS_2/WSSe vdW heterojunctions can thus be used as promising candidates for designing the next generation nanoelectronic and optoelectronic devices.

Acknowledgments

This work was financially supported by the National Nature Science Foundation of China (61888102), the National Key Research and Development Projects of China (2016YFA0202300), the Strategic Priority Research Program of the Chinese Academy of Sciences (XDB30000000), and the Fundamental Research Funds for the Central Universities.

Data availability statement

The data that support the findings of this study are available upon reasonable request from the authors.

ORCID iDs

Yan-Fang Zhang https://orcid.org/0000-0002-9669-104X
Jinbo Pan https://orcid.org/0000-0003-2612-8232
Shixuan Du https://orcid.org/0000-0001-9323-1307

References

[1] Mak K F, Lee C, Hone J, Shan J and Heinz T F 2010 Atomically thin MoS_2: a new direct-gap semiconductor *Phys. Rev. Lett.* **105** 136805
[2] Mak K F and Shan J 2016 Photonics and optoelectronics of 2D semiconductor transition metal dichalcogenides *Nat. Photon.* **10** 216–26
[3] Gan Z X, Liu L Z, Wu H Y, Hao Y L, Shan Y, Wu X L and Chu P K 2015 Quantum confinement effects across two-dimensional planes in MoS_2 quantum dots *Appl. Phys. Lett.* **106** 233113
[4] Wang S and Wang J 2015 Spin and valley half-metal state in MoS_2 monolayer *Physica* B **458** 22–6
[5] Wang S, Ukhtary M S and Saito R 2020 Strain effect on circularly polarized electroluminescence in transition metal dichalcogenides *Phys. Rev. Res.* **2** 033340
[6] Zhang H 2015 Ultrathin two-dimensional nanomaterials *ACS Nano* **9** 9451–69
[7] Das S, Kim M, Lee J W and Choi W 2014 Synthesis, properties, and applications of 2D materials: a comprehensive review *Crit. Rev. Solid State Mater. Sci.* **39** 231–52
[8] Zhang C M, Nie Y H, Sanvito S and Du A J 2019 First-principles prediction of a room-temperature ferromagnetic Janus VSSe monolayer with piezoelectricity, ferroelasticity, and large valley polarization *Nano Lett.* **19** 1366–70
[9] Splendiani A, Sun L, Zhang Y B, Li T S, Kim J, Chim C Y, Galli G and Wang F 2010 Emerging photoluminescence in monolayer MoS_2 *Nano Lett.* **10** 1271–5
[10] Kim S *et al* 2012 High-mobility and low-power thin-film transistors based on multilayer MoS_2 crystals *Nat. Commun.* **3** 1011
[11] Janisch C, Song H M, Zhou C J, Lin Z, Elias A L, Ji D X, Terrones M, Gan Q Q and Liu Z W 2016 MoS_2 monolayers on nanocavities: enhancement in light–matter interaction *2D Mater.* **3** 025017
[12] Peng Q, Wang Z Y, Sa B S, Wu B and Sun Z M 2016 Electronic structures and enhanced optical properties of blue phosphorene/transition metal dichalcogenides van der Waals heterostructures *Sci. Rep.* **6** 31994
[13] Bernardi M, Ataca C, Palummo M and Grossman J C 2017 Optical and electronic properties of two-dimensional layered materials *Nanophotonics* **6** 479–93
[14] Zhang Z H, Liu X F, Yu J, Hang Y, Li Y, Guo Y F, Xu Y, Sun X, Zhou J X and Guo W L 2016 Tunable electronic and magnetic properties of two-dimensional materials and their one-dimensional derivatives *Wiley interdiscip. Rev.: Comput. Mol. Sci.* **6** 324–50
[15] Zhao P L, Yu J, Zhong H, Rosner M, Katsnelson M I and Yuan S J 2020 Electronic and optical properties of transition metal dichalcogenides under symmetric and asymmetric field-effect doping *New J. Phys.* **22** 083072
[16] Lee C H *et al* 2014 Atomically thin p-n junctions with van der Waals heterointerfaces *Nat. Nanotechnol.* **9** 676–81
[17] Wu W Z *et al* 2014 Piezoelectricity of single-atomic-layer MoS_2 for energy conversion and piezotronics *Nature* **514** 470–4
[18] Li M Y, Chen C H, Shi Y M and Li L J 2016 Heterostructures based on two-dimensional layered materials and their potential applications *Mater. Today* **19** 322–35
[19] Li C L, Cao Q, Wang F Z, Xiao Y Q, Li Y B, Delaunay J J and Zhu H W 2018 Engineering graphene and TMDs based van der Waals heterostructures for photovoltaic and photoelectrochemical solar energy conversion *Chem. Soc. Rev.* **47** 4981–5037
[20] Wang C Y, Yang F C and Gao Y H 2020 The highly-efficient light-emitting diodes based on transition metal dichalcogenides: from architecture to performance *Nanoscale Advances* **2** 4323–40
[21] Palacios-Berraquero C *et al* 2016 Atomically thin quantum light-emitting diodes *Nat. Commun.* **7** 12978
[22] Cui Z, Bai K, Ding Y, Wang X, Li E and Zheng J 2020 Janus XSSe/SiC (X = Mo, W) van der Waals heterostructures as promising water-splitting photocatalysts *Physica* E **123** 114207
[23] Ren K, Yu J and Tang W 2020 Two-dimensional ZnO/BSe van der waals heterostructure used as a promising photocatalyst for water splitting: a DFT study *J. Alloys Compd.* **812** 152049
[24] Li J, Huang Z, Ke W, Yu J, Ren K and Dong Z 2021 High solar-to-hydrogen efficiency in Arsenene/GaX (X = S, Se) van der Waals heterostructure for photocatalytic water splitting *J. Alloys Compd.* **866** 158774
[25] Guan Z, Lian C-S, Hu S, Ni S, Li J and Duan W 2017 Tunable structural, electronic, and optical properties of layered two-dimensional C_2N and MoS_2 van der Waals heterostructure as photovoltaic material *J. Phys. Chem.* C **121** 3654–60
[26] Guan Z, Ni S and Hu S 2018 Tunable electronic and optical properties of monolayer and multilayer Janus MoSSe as a photocatalyst for solar water splitting: a first-principles study *J. Phys. Chem.* C **122** 6209–16
[27] Nourbakhsh A, Zubair A, Dresselhaus M S and Palacios T 2016 Transport properties of a MoS_2/WSe_2 heterojunction transistor and its potential for application *Nano Lett.* **16** 1359–66
[28] Rivera P *et al* 2015 Observation of long-lived interlayer excitons in monolayer $MoSe_2$–WSe_2 heterostructures *Nat. Commun.* **6** 6242
[29] Ceballos F, Bellus M Z, Chiu H Y and Zhao H 2014 Ultrafast charge separation and indirect exciton formation in a MoS_2–$MoSe_2$ van der Waals heterostructure *ACS Nano* **8** 12717–24
[30] Wang T, Jin H, Li J W and Wei Y D 2018 Toward barrier free contact to $MoSe_2/WSe_2$ heterojunctions using two-dimensional metal electrodes *Nanotechnology* **30** 015707
[31] Jin C H *et al* 2019 Observation of moire excitons in WSe_2/WS_2 heterostructure superlattices *Nature* **569** 76–80
[32] Trivedi D B *et al* 2020 Room-temperature synthesis of 2D Janus crystals and their heterostructures *Adv. Mater.* **32** 2006320
[33] Lin Y C *et al* 2020 Low energy implantation into transition-metal dichalcogenide monolayers to form Janus structures *ACS Nano* **14** 3896–906
[34] Li F P, Wei W, Zhao P, Huang B B and Dai Y 2017 Electronic and optical properties of pristine and vertical and lateral heterostructures of Janus MoSSe and WSSe *J. Phys. Chem. Lett.* **8** 5959–65
[35] Guo W Y, Ge X, Sun S T, Xie Y Q and Ye X 2020 The strain effect on the electronic properties of the MoSSe/WSSe van der Waals heterostructure: a first-principles study *Phys. Chem. Chem. Phys.* **22** 4946–56
[36] Zhou Z B, Niu X H, Zhang Y H and Wang J L 2019 Janus MoSSe/WSeTe heterostructures: a direct Z-scheme photocatalyst for hydrogen evolution *J. Mater. Chem.* A **7** 21835–42

[37] Idrees M, Din H U, Ali R, Rehman G, Hussain T, Nguyen C V, Ahmad I and Amin B 2019 Optoelectronic and solar cell applications of Janus monolayers and their van der Waals heterostructures *Phys. Chem. Chem. Phys.* **21** 18612–21

[38] Kresse G and Furthmüller J 1996 Efficient iterative schemes for *ab initio* total-energy calculations using a plane-wave basis set *Phys. Rev.* B **54** 11169

[39] Kresse G and Joubert D 1999 From ultrasoft pseudopotentials to the projector augmented-wave method *Phys. Rev.* B **59** 1758

[40] Kresse G and Furthmüller J 1996 Efficiency of ab-initio total energy calculations for metals and semiconductors using a plane-wave basis set *Comput. Mater. Sci.* **6** 15–50

[41] Krukau A V, Vydrov O A, Izmaylov A F and Scuseria G E 2006 Influence of the exchange screening parameter on the performance of screened hybrid functionals *J. Chem. Phys.* **125** 224106

[42] Klimes J, Bowler D R and Michaelides A 2011 Van der Waals density functionals applied to solids *Phys. Rev.* B **83** 195131

[43] Neugebauer J and Scheffler M 1992 Adsorbate-substrate and adsorbate-adsorbate interactions of Na and K adlayers on Al(111) *Phys. Rev.* B **46** 16067–80

[44] Baroni S and Resta R 1986 *Ab initio* calculation of the macroscopic dielectric constant in silicon *Phys. Rev.* B **33** 7017–21

[45] Gajdos M, Hummer K, Kresse G, Furthmuller J and Bechstedt F 2006 Linear optical properties in the projector-augmented wave methodology *Phys. Rev.* B **73** 045112

[46] Xu Y, Li Y, Chen X, Zhang C F, Zhang R and Lu P F 2016 First-principle study of hydrogenation on monolayer MoS_2 *AIP Adv.* **6** 075001

[47] Xu M L, Chen Y, Xiong F, Wang J Y, Liu Y H, Lv J, Li Y W, Wang Y C, Chen Z F and Ma Y M 2018 A hidden symmetry-broken phase of MoS_2 revealed as a superior photovoltaic material *J. Mater. Chem.* A **6** 16087–93

[48] Ju L, Bie M, Tang X, Shang J and Kou L Z 2020 Janus WSSe monolayer: an excellent photocatalyst for overall water splitting *ACS Appl. Mater. Interfaces* **12** 29335–43

[49] Huang H W *et al* 2020 Direct Z-scheme heterojunction of semicoherent $FAPbBr_3/Bi_2WO_6$ interface for photoredox reaction with large driving force *ACS Nano* **14** 16689–97

[50] Torun E, Miranda H P C, Molina-Sánchez A and Wirtz L 2018 Interlayer and intralayer excitons in MoS_2/WS_2 and $MoSe_2/WSe_2$ heterobilayers *Phys. Rev.* B **97** 245427

[51] Feng J, Qian X F, Huang C W and Li J 2012 Strain-engineered artificial atom as a broad-spectrum solar energy funnel *Nat. Photon.* **6** 865–71

[52] Conley H J, Wang B, Ziegler J I, Haglund R F, Pantelides S T and Bolotin K I 2013 Bandgap engineering of strained monolayer and bilayer MoS_2 *Nano Lett.* **13** 3626–30

[53] Li X F *et al* 2016 Two-dimensional $GaSe/MoSe_2$ misfit bilayer heterojunctions by van der Waals epitaxy *Sci. Adv.* **2** e1501882

[54] Yang C W, Tang H L, Sattar S, Chiu M H, Wan Y, Chen C H, Kong J, Huang K W, Li L J and Tung V 2020 Epitaxial growth and determination of band alignment of Bi_2Te_3–WSe_2 Vertical van der Waals Heterojunctions *ACS Mater. Lett.* **2** 1351–9

[55] Peng X, Wei Q and Copple A 2014 Strain-engineered direct-indirect band gap transition and its mechanism in two-dimensional phosphorene *Phys. Rev.* B **90** 085402